Supporting Information

Rego et al. 10.1073/pnas.1107547108

SI Materials and Methods.

Photobleaching Studies. Photobleaching studies were done in fixed CHO cells, expressing Dronpa cytosolically. Cells were fixed with 1% PFA in PHEM buffer (60 mM PIPES; 25 mM HEPES; 10 mM EGTA; and 2 mM MgCl2, pH 6.9). They were then mounted in PHEM buffer or 5 mM p-phenylenediamine (PPD) in PHEM buffer adjusted with NaOH to maintain pH 6.9.

Dronpa Purification and Biotinylation. Dronpa was purified using standard methods. Briefly, the gene was purchased from MBL, subcloned into a standard His-tag purification vector pSV271 (gift from D. Minor, University of California, San Francisco, CA), expressed in *Escherichia coli*, purified using gravity over a prepacked nickel column (GE Healthcare), and eluted using imidazole. The protein was then snap frozen in 5% glycerol and stored at −80 °C.

NHS-PEG_4-biotin ester was purchased from Pierce (catalog no. 21329), and conjugated to Dronpa in PBS, pH 7.5, at room temperature under gentle agitation for 2 h. The free ester was separated from the protein with two size exclusion columns (7 kDa and 100 kDa molecular weight cut-off) in a fixed-angle rotor and once in a swinging bucket rotor using the size exclusion columns supplied with the Invitrogen biotinylation kit (catalog no. D-20655).

Dronpa-Coated Microtubules. Biotinylated tubulin purchased from Cytoskeleton, Inc. was polymerized in BRB80 buffer (80 mM PIPES; 1 mM EGTA; and 1 mM MgCl2, pH 6.8) with 1 mM GTP and 10% glycerol for 30 min at 37 °C. To stabilize the microtubules, taxol was gradually added to a final concentration of 10 μM during the 30 min. Microtubules were pelleted at 600,000 × *g* for 15 min at 37 °C in a fixed-angle rotor over a solution of warm buffered 40% glycerol. The pellets were resuspended in warm BRB80 supplemented with 1 mM GTP and 20 μM taxol. These microtubules were passed through a 30-gauge needle four to six times, pelleted and resuspended as above. To prepare the samples, flow chambers were constructed between two coverslips using double-sided tape.

Square 25-mm and round 18-mm coverslips were sonicated in 1 M KOH followed by sonication in Millipore water, each for 1 h, rinsed again in Millipore water, and finally kept in a covered dish filled with Millipore water until use. Directly prior to use, the coverslips were immersed in 200-proof ethanol and dried by a pure stream of ionized Nitrogen air. Poly-d-lysine (Sigma catalog no. P1149) was diluted to 1 mg/mL in water and allowed to coat the coverslip for 30–90 min. The surface was washed extensively with BRB80 buffer containing 1 mM GTP and 20 μM taxol. Microtubules were diluted to an appropriate concentration in this same buffer and allowed to diffuse to the surface for at least 1 h. The chambers were then washed with buffer containing 1 mg/mL casein from bovine milk (Sigma catalog no. 7078) to prevent nonspecific binding of proteins to the glass surface; the last wash was incubated for 15 min. All reactions and dilutions that follow were carried out in BRB80 buffer containing 1 mM GTP, 20 μM taxol, and 1 mg/mL casein. Streptavidin (Invitrogen catalog no. S888) was diluted to a final concentration of 0.2 mg/mL or 1 mg/mL and incubated for 15 min. The samples were again washed extensively with buffer, and biotinylated Dronpa was added and allowed to bind for 15 min. The coated microtubules were washed a final time. To prevent photobleaching, 5 mM PPD was added, and the ends of the flow chambers were sealed with nail polish (Sally Hansen Hard as Nails) or VALAP. The underside of the objective was cleaned with water and ethanol and then affixed to a metal slide using small magnets.

Cell Culture. CHO cells were cultured using standard protocols and transfected with Dronpa–Lifeact using Amaxa transfection reagents. Six to ten hours after transfection, the cells were typsinized and plated at lower density on clean coverslips to induce spreading. Cells were fixed 48 h after this for 10 min with 1% PFA in PHEM containing 1 μM unlabelled phalloidin (1). They were then mounted in 5 mM PPD in PHEM, sealed from air, and imaged. Cells used in the photobleaching study were transfected with Dronpa cytosolically, allowed to express for 20 h, and then fixed in 1% PFA in PHEM for 20 min.

Nuclear Isolation. HEK293 cells cultured in 10-cm dishes were transfected with 12-μg Dronpa-Nup98 plasmid and 30 μL Lipofectamine 2000 reagent (Invitrogen catalog no. 11668). Forty-eight hours after transfection, cells from two plates were harvested by scraping and pelleted in PBS. The cells were then resuspended in 1 mL ice-cold Glycerophosphate buffer (10 mM glycerophosphate, pH 7.0; 2 mM $MgCl_2$) and placed on ice for 7 min. After 7 min, 1 mL of ice-cold water was added, and the cells were placed on ice for an additional 7 min. The cells were then dounced until broken, and 2 mL of ice-cold Glycerol Stabilization Buffer (100 mM Glycerophostphate, pH 7.0; 2 mM $MgCl_2$; and 40% glycerol) was added. This lysate was centrifuged at 1,000 × *g* for 10 min at 4 °C over a cold sucrose cushion. The sucrose cushion was preassembled by layering 6 mL of 340 mM sucrose over 6 mL of 500 mM sucrose, each buffered with 65 mM glycerophosphate, pH 7.0 with 2 mM sucrose and 20% glycerol. The pellet containing the nuclei was resuspended in a final storage buffer consisting of 10 mM glycerophosphate buffer, pH 7.0, 2 mM $MgCl_2$, 25 mM KCl, and 0.34 M sucrose. The nuclei were immediately fixed by adding PFA to a final concentration of 2% and placed on ice for 10 min. The fixed nuclei were again centrifuged over a sucrose cushion and resuspended in the storage buffer. Finally, nuclei were allowed to settle on poly-d-lysine coated coverslips for 1 h at 4 °C, washed with PHEM buffer, and mounted in 5 mM PPD in PHEM at pH 6.9.

Plasmid Preparation. pEGFP-Nup98 and pPOM121-EGFP3 were courtesy of the Ellenberg lab through Euroscarf (http://web.uni-frankfurt.de/fb15/mikro/euroscarf/). We subcloned the Dronpa gene into the pEGFP-Nup98 vector using the AgeI and BglII restrictions sites with the following forward and reverse PCR primers: (Forward) CTAGCGCTACCGGTCGCCACCATGGTG-AGTGTGATTAAACCAGAC; (Reverse) GCTCGAGATCTG-AGTCCGGCCGGACTTGGCCTGCCTCGGCAGCTCAGA.

The POM121-Dronpa plasmid was constructed by first performing overlap extension PCR to add the nucleic acid sequence of the terminal 23 amino acids of POM121 to the 5′ end of the DRONPA cDNA. The PCR reaction also introduced BamHI and XbaI restriction enzyme sites that were for ligation into the plasmid pPOM121-EGFP3. The primer set consisted of the following:

Dronpa-F1 (5′-atggaccggtcgccacc**ATG**GTGAGTGTGATTA-AACCAGACAT-3′)

POM-F1 (5′-cccgcaagaagggaggcgggggcaatggaccggtcgccaccA-TGG-3′)

POM-F2 (5-cgacttcaggcccgaaggcagcacacccgcaagaagggaggcg-gg-3′)

POM-F3 (5′-gatccaagaccccaggggctcgacagcgacttcaggcccgaag-gc-3′)

POM-F4 (5′-ttggcgcgggatccaagaccccaggggctcgacagcgacttc-3)

Dronpa-R1 (5′ atgatctagagtcgcggccgct**TTA**CTTGGCCTGCC-TCGGCAGC-3′

BamHI and XbaI restriction enzyme recognition sequences are underlined, and sequences corresponding to start and stop of the Dronpa coding sequence are indicated by bold print.

pLifeact–Dronpa was cloned using a Clontech-style N1 EGFP cloning vector where EGFP was replaced with Dronpa using AgeI and NotI restriction sites with the following forward and reverse primers: (Forward) GCTAGCGCTACCGGTCGCCACCATG-GTGAGTGTGATTAAACCAGACATGAAG; (Reverse) CATT-CTGAGCTGCCGAGGCAGGCCAAGTAAGCGGCCGCGA-CTCTAG. The resulting Dronpa-N1 cloning vector was cut with NheI and BamHI followed by ligation with a duplex oligonucleotide encoding the Lifeact sequence: (Forward) CTAGCGCCAC-CATGGGCGTGGCCGACTTGATCAAGAAGTTCGAGTCC-ATCTCCAAGGAGGAGGGG; (Reverse) GATCCCCCTCC-TCCTTGGAGATGGACTCGAACTTCTTGATCAAGTCGG-CCACGCCCATGGTGGCG. The final products were confirmed by sequencing. All plasmids were prepped using an endo-free Maxi kit from Qiagen, and eluted in water to a final concentration around 1 μg/μL.

Intensity Calibration and Conditions. Because we confirmed that the off-rate of Dronpa was linearly proportional to the intensity of the 488-nm light (Fig. S1*A*), we used this rate to infer the intensity of the total internal reflection fluorescence (TIRF) illumination, which could not be directly measured. For this measurement, we chose to use the Dronpa-coated microtubules because they represented a purely two-dimensional sample. First, we measured the off-rate under illumination with the central order of the diffraction grating. With this order, we could directly measure the power coming out of the objective and thus calculate the intensity. We then measured the off-rate under TIRF illumination with the −1 diffraction order beam; this allowed us to infer the intensity of TIRF illumination. We next measured the power at a conjugate image plane behind the tube lens for the −1 diffraction order and used this as our measure of the TIRF intensity in all experiments. For each nonlinear structured-illumination microscopy (NL-SIM) experiment, the rate constant was measured on the region to be imaged or on a nearby region directly prior to data collection. The power was then adjusted to produce the desired rate constant (typically 1–2 s) under illumination with the pattern, noting that the intensity at the peak of the pattern was four times higher than the intensity with uniform illumination with just one side order. Typically, the 488-nm power was adjusted to approximately 50 μW at the conjugate image plane corresponding to an intensity of approximately 5 W/cm^2 at the peak of the pattern in the TIRF zone and an off-time of 1–1.5 s. The samples were turned off by roughly a saturation factor of 8–15 and exposed for a factor of 5. We used the same calibration factor to calculate the intensity of the 405-nm activation light. The activation energy required to turn on 2/3 of the molecules was measured to be approximately 40 mJ/cm^2. We chose to saturate the on state completely during imaging with activation energies of approximately 0.5–1 J/cm^2, observing no correlation between the number of photoswitching cycles versus the activation energy at and above saturation.

Images and Figures. Images were analyzed with IVE Priism and ImageJ; Fig. 1 was generated by Mathematica; traces were analyzed and plotted using Igor Pro. All images were assembled in Adobe Illustrator.

SI Discussion.

The point-spread function (PSF) describes the response of the imaging system to a point source of light: It maps the emission distribution of the sample to the intensity distribution on the detector. Thus, an image of any object is a convolution between the PSF and the emission intensity:

$$D(\mathbf{x}) = (\mathrm{Em} \otimes P)(\mathbf{x}), \quad \textbf{[S1]}$$

where $D(\mathbf{x})$ is the distribution of photons on the detector, $\mathrm{Em}(\mathbf{x})$ is the emission distribution of the sample, $P(\mathbf{x})$ is the PSF of the microscope, and $\otimes$ denotes a convolution operation. Taking the Fourier transform and using the convolution theorem, we obtain an expression describing the spatial frequencies accessible to the microscope:

$$\tilde{D}(\mathbf{k}) = \tilde{\mathrm{Em}}(\mathbf{k}) \cdot \mathrm{OTF}(\mathbf{k}), \quad \textbf{[S2]}$$

where the tilde indicates the Fourier transform of the function and optical transfer function (OTF) is the Fourier transform of the PSF. In conventional fluorescence microscopy, the emission distribution itself is the local product of the illumination, I, and the sample fluorescence, S, distributions:

$$\mathrm{Em}(\mathbf{x}) = I(\mathbf{x}) \cdot S(\mathbf{x}), \quad \textbf{[S3]}$$

or equivalently in frequency-space:

$$\tilde{\mathrm{Em}}(\mathbf{k}) = (\tilde{I} \otimes \tilde{S})(\mathbf{k}). \quad \textbf{[S4]}$$

Rearranging Eq. **S2**, we obtain the Fourier transform of the observed image:

$$\tilde{D}(\mathbf{k}) = (\tilde{I} \otimes \tilde{S})(\mathbf{k}) \cdot \mathrm{OTF}(\mathbf{k}). \quad \textbf{[S5]}$$

In conventional wide-field microscopy, the sample is uniformly illuminated, meaning that $\tilde{I}(\mathbf{k})$ is a delta function at the origin. In this case, Eq. **S5** becomes

$$\tilde{D}(\mathbf{k}) = \tilde{S}(\mathbf{k}) \cdot \mathrm{OTF}(\mathbf{k}), \quad \textbf{[S6]}$$

and we observe that the spatial frequencies attainable by a microscope with uniform illumination are limited by the cutoff frequency of the OTF, which is under ideal conditions described by the Abbé limit. However, if the illumination is nonuniform, like in structured-illumination microscopy (SIM), then Eq. **S6** does not hold.

Linear SIM. Consider a case that uses a one-dimensional sinusoidal-varying pattern of light as the illumination source. The illumination can then be described as

$$I(\mathbf{x}) = \frac{I_0}{2}(1 - \cos(2\pi k_0 \mathbf{x} + \varphi)), \quad \textbf{[S7]}$$

where k_0 and φ are the spatial frequency and the phase of the illumination pattern, respectively, and I_0 is the peak illumination intensity. By Fourier transforming Eq. **S7** and substituting into Eq. **S5**, we are left with an expression for the observed image:

$$\tilde{D}(\mathbf{k}) = \frac{I_0}{2}\left[\tilde{S}(\mathbf{k}) - \frac{1}{2}\tilde{S}(\mathbf{k}-k_0)e^{-i\varphi} - \frac{1}{2}\tilde{S}(\mathbf{k}+k_0)e^{+i\varphi}\right]\mathrm{OTF}(\mathbf{k}). \quad \textbf{[S8]}$$

The first term in Eq. **S8** represents all the spatial frequencies normally observed by the microscope (Eq. **S6**), but the last two terms contribute new information. These terms are only observed in the region of frequency space where OTF($\mathbf{k}$) is nonzero, except now their origins have been shifted in frequency space by k_0 such that part of the information they encode resides outside the normally supported observable region. By obtaining three images with three different phases, φ, of the illumination pattern we can obtain a system of three independent linear equations, which allows us to separate the three terms in Eq. **S8**. Lastly, to obtain nearly isotropic resolution in two dimensions, the one-dimensional pattern must be rotated in at least three orientations. In this way, it is possible to increase the resolution of a light microscope by a factor of approximately 2.

Nonlinear Structured-Illumination Imaging. Eq. **S3** above assumes that the emission rate of the sample is linearly proportional to the illumination intensity. This is a valid assumption for most fluorescence microscopy. However, there are many known nonlinear fluorescence phenomenon: two-photon absorption, stimulated emission, ground state depletion, saturation, and photoswitching, among others. Before discussing one of these phenomena in detail, consider a yet-to-be-described nonlinear photophysical process. Then, Eq. **S3** becomes

$$\mathrm{Em}(\mathbf{x}) = F[I(\mathbf{x})] \cdot S(\mathbf{x}), \quad \textbf{[S9]}$$

where F describes the nonlinear behavior of the sample in response to the illumination light. First, assume the nonlinearity is nonpolynomial, which can be expressed as a power series with an infinite number of terms:

$$F[I(\mathbf{x})] = a_0 + a_1 I(\mathbf{x}) + a_2 I^2(\mathbf{x}) + a_3 I^3(\mathbf{x}) + \ldots \quad \textbf{[S10]}$$

Again, consider the case of a one-dimensional sinusoidal illumination pattern. Then, Eq. **S10** becomes

$$F[I(\mathbf{x})] = b_0 + b_1\cos(2\pi k_0\mathbf{x} + \varphi) + b_2\cos(4\pi k_0\mathbf{x} + 2\varphi) + b_3\cos(6\pi k_0\mathbf{x} + 3\varphi) + \ldots \quad \textbf{[S11]}$$

After transforming Eq. **S11** to frequency space and substituting the result into Eq. **S5**, we find that the data takes the form of a weighted sum of an infinite number of components:

$$\tilde{D}(\mathbf{k}) = \mathrm{OTF}(\mathbf{k}) \sum_{m=-\infty}^{\infty} b_m \tilde{S}(\mathbf{k} - mk_0)e^{-im\varphi}. \quad \textbf{[S12]}$$

Comparing this function to the same result for linear fluorescence (Eq. **S8**), we see that the $m = -1,1,0$ terms contain all the information from both the conventional OTF and the extended linear structured-illumination OTF. Importantly, **[S12]** also contains an infinite number of higher-order harmonics at integer multiples of the fundamental spatial frequency. Of course, no imaging system is perfect: There will only be a finite number, N, of the higher-order information components that are able to rise above the noise because the power series coefficients in Eq. **S10** successively decrease. Similar to the separation of the linear structured-illumination raw data, it is possible to separate the higher-order information components if $2N + 1$ images are taken at different phases of the illumination pattern. Again, the one-dimensional pattern needs to be rotated in a sufficient number of orientations in order to fill the entire two-dimensional space isotropically.

NL-SIM with Photoswitchable Molecules. We now consider the results above in relation to a specific nonlinear phenomenon—photoswitching. Each image used during processing is a result of three exposures.

i. Turn on. Because of lateral chromatic aberration between the activation light and the excitation light, we chose to turn the sample on uniformly.
ii. Turn off. Assume a one-dimensional sinusoidally varying pattern of light that drives the molecules to the off state. This can be again be described as

$$I_{\mathrm{off}} = \frac{I_0}{2}(1 - \cos(2\pi k_0\mathbf{x} + \varphi)). \quad \textbf{[S13]}$$

After some time, T, the distribution of molecules remaining on will be

$$S_{\mathrm{on}}(\mathbf{x}) = e^{-\frac{T}{I_0\tau_{\mathrm{off}}}I_{\mathrm{off}}(\mathbf{x})}S(\mathbf{x}), \quad \textbf{[S14]}$$

where τ_{off} is the characteristic time to the off state and $S(\mathbf{x})$ is the sample distribution itself. We define the term saturation level, η, to be the ratio of the exposure time T to the time constant τ_{off}. Eq. **S2** then becomes

$$S_{\mathrm{on}}(\mathbf{x}) = e^{-\eta(1-\cos(2\pi k_0\mathbf{x}+\varphi))}S(\mathbf{x}). \quad \textbf{[S15]}$$

iii. Expose. Let us first consider the most general case in which the remaining on molecules are observed under uniform illumination, which only excites but does not drive the molecules to the dark state. In this case,

$$\mathrm{Em}(\mathbf{x})I_0 \cdot S_{\mathrm{on}}(\mathbf{x}) = I_0 e^{-\frac{\eta}{I_0}I_{\mathrm{off}}(\mathbf{x})}S(\mathbf{x}) = I_0 e^{-\frac{\eta}{2}(1-\cos(2\pi k_0\mathbf{x}+\varphi))}S(\mathbf{x}). \quad \textbf{[S16]}$$

Comparing Eq. **S16** to Eq. **S9**, we find that photoswitching produces the desired nonlinear response. That is,

$$F[I_{\mathrm{off}}(\mathbf{x})] = e^{-\frac{\eta}{I_0}I_{\mathrm{off}}(\mathbf{x})}I_0. \quad \textbf{[S17]}$$

Using the approximation

$$1 - \cos(2\pi k_0\mathbf{x} + \varphi) \approx \frac{(2\pi k_0 + \varphi)^2}{4}, \quad \textbf{[S18]}$$

Eq. **S16** can be well approximated around the region $2\pi k_0\mathbf{x} + \varphi = 0$ as a Gaussian distribution:

$$\mathrm{Em}(\mathbf{x}) \approx e^{-\frac{\eta}{4}(2k_0\pi\mathbf{x}+\varphi)^2}I_0 S(\mathbf{x}), \quad \textbf{[S19]}$$

with a full width at half maximum (FWHM) of

$$\Delta\chi_{\mathrm{FWHM}} = \frac{2\sqrt{\ln 2}}{k_0\pi\sqrt{\eta}}. \quad \textbf{[S20]}$$

The numerical approximation (Eq. **S19**) agrees well with the complete solution at moderate to high saturation level (Fig. S9*A*). From Eq. **S20**, we can see that at high saturation

level, the FWHM of the peaks of the patterned-on molecules can be much smaller than the diffraction limit. We also observe why it is advantageous to use a high spatial frequency, k_0, of the illumination pattern.

Now, let us consider our specific case in which we collect the remaining fluorescence from the on molecules by shifting the illumination pattern over by π:

$$I_{\text{exp}}(\mathbf{x}) = \frac{I_0}{2}(1 - \cos(2\pi k_0 \mathbf{x} + (\varphi + \pi))). \qquad \textbf{[S21]}$$

Moreover, the photoswitchable molecule Dronpa we chose to use in our study is excited and driven to the off state with the same wavelength of light. Consequently, while the fluorescence is being detected, the molecules will be driven to the dark state. The total normalized integrated emission for an exposure time T_2, or equivalently, for a saturation factor η_2 will then be

$$\text{Em}(\mathbf{x}) = \frac{1}{\tau_{\text{off}}} \int_0^{T_2} I_{\text{exp}}(\mathbf{x}) e^{\frac{-t}{\tau_{\text{off}} I_0} I_{\text{exp}}(\mathbf{x})} S(\mathbf{x}) dt$$

$$\text{Em}(\mathbf{x}) = \int_0^{\eta_2} I_{\text{exp}}(\mathbf{x}) e^{-\eta[1-\cos(2\pi k_0 \mathbf{x} + (\varphi+\pi))]} S_{\text{on}}(\mathbf{x}) d\eta. \qquad \textbf{[S22]}$$

At low saturation ($\eta = 2$), the effect of the patterned excitation light is noticeable because the zero of the excitation light will affect the nonzero trough of the patterned-on molecules. However, at higher saturation ($\eta = 10$), there is little to no difference between patterned and uniform excitation because such high saturation creates a nearly perfect zero of the on-state pattern assuming infinite contrast ratios (Fig. S9*B*). For more realistic contrast ratios of tens to thousands, the effect of the patterned excitation light may be more pronounced and beneficial.

1. Svitkina T, et al. (2003) Mechanism of filopodia initiation by reorganization of a dendritic network. *J Cell Biol* 160:409–421.

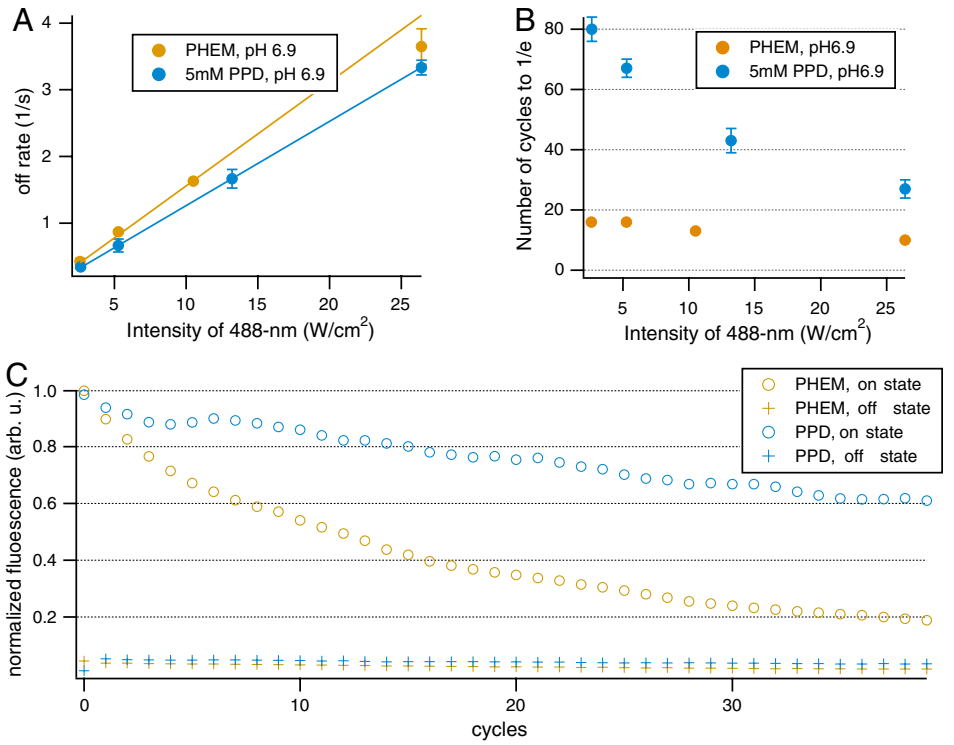

Fig. S1. Photoswitching and photobleaching characteristics of Dronpa. (*A*) Under illumination with 488-nm light, Dronpa decays to a reversible dark state with a characteristic off-rate. As expected, the off-rate of Dronpa is linear with illumination intensity and does not change substantially with the addition of PPD. (*B*) With the exposure time, T, controlled for the same saturation factor ($\eta = 5$; $T = \eta$/off-rate), the number of cycles before photobleaching to $1/e$ dramatically increased at lower light intensity and the addition of PPD (blue dots). A characteristic cycling curve is shown in *C* at an intensity of 2.6 W/cm^2. The fluorescence from Dronpa is longer lived in the on state with the addition of PPD versus PHEM buffer at the same pH (open circles). Importantly, the background in the off state does not increase significantly (crosses).

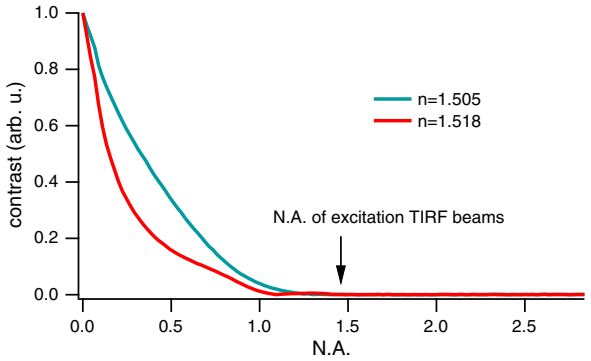

Fig. S2. OTF at different indices of refraction. The OTF of the 100 × /1.46 N.A. TIRF objective was measured by imaging a single 100-nm fluorescent bead. This image was transformed to frequency space, the result rotationally averaged, and the singularity at the origin suppressed. We did this process using immersion oil with an index of refraction of 1.518 and then using oils with successively lower indices of refraction until the high-frequency content of the transfer function was optimized. Not only does optimizing the high-frequency content provide higher resolution because the extent of the conventional OTF has been maximized, but it also provides greater overlap between all the information components, allowing for a greater reliability in the fit parameters (pattern vector, scaling factors of higher orders, etc.) during processing and providing more isotropic resolution as the extended OTF gets larger. However, even in the optimized immersion liquid, the N.A. of the excitation beams still falls well outside the detection OTF, generating an ultrafine period of 166 nm. This is possible because the coherent illumination source (a single-mode fiber) transmits these high spatial frequencies with almost perfect modulation (95–96.5%).

A

Number of higher order hamonics	Expected Resolution	Number of images in one dimension	Number of images in two dimensions
0 (linear SIM)	94-nm	3	9
1	63-nm	5	25
2	47-nm	7	49
6	24-nm	15	225

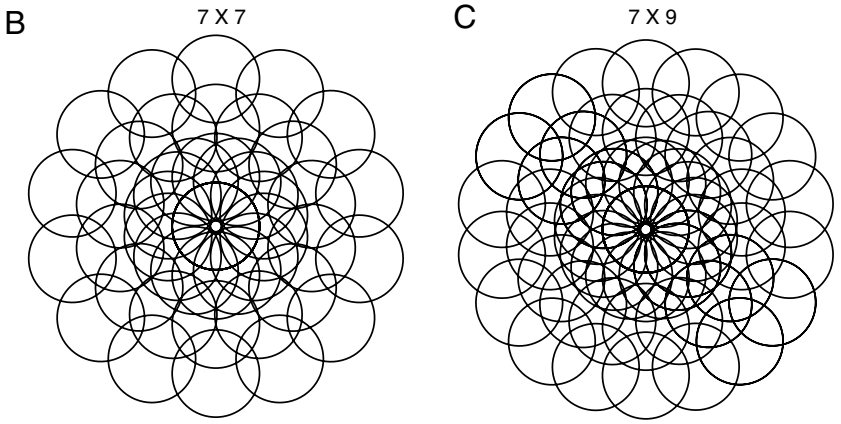

Fig. S3. Expected resolution with NL-SIM for different number of information components. (*A*) The nominal expected resolution, as more higher-order harmonics are added to the transfer function. These numbers assume an effective detection N.A. of 1.3, an illumination N.A. of 1.46, and a detection wavelength of 525 nm. The number of images in one dimension is the number of phases needed to properly unmix the information components. The minimum number of images in two dimensions is the number of images needed to fill the two-dimensional space. Using more orientations of the pattern fills the space more isotropically. This is illustrated with seven phases and seven pattern orientations (*B*) or seven phases and nine pattern orientations (*C*).

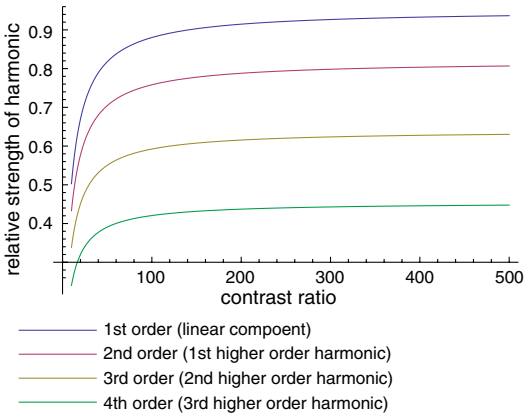

Fig. S4. Harmonic strength versus contrast ratio. To understand how the contrast ratio affects the signal strength in the higher-order harmonics we modeled the simple and worst case scenario of uniform illumination exposure (see *SI Discussion*). In this case and using $\eta = 10$, contrast ratios above >50 have little to no effect on the relative strength of the higher-order information components compared to the conventional component.

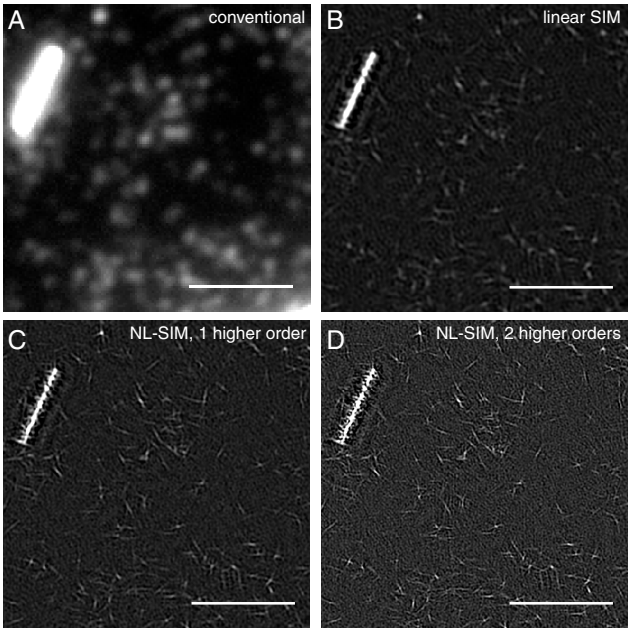

Fig. S5. Stochastic single molecules. The contrast of the images was greatly enhanced to make the single molecules in the background visible over the well-coated and bright microtubule. The single molecules in the background are not reliably on or reliably off during imaging. After the processing, they appear in our images as being narrow in just a few directions and broad in others, giving them a streak-like appearance. Importantly, this effect can also be seen on the microtubules as the resolution increases and the number of molecules per pixel decreases. Scale bar, 2 μm.

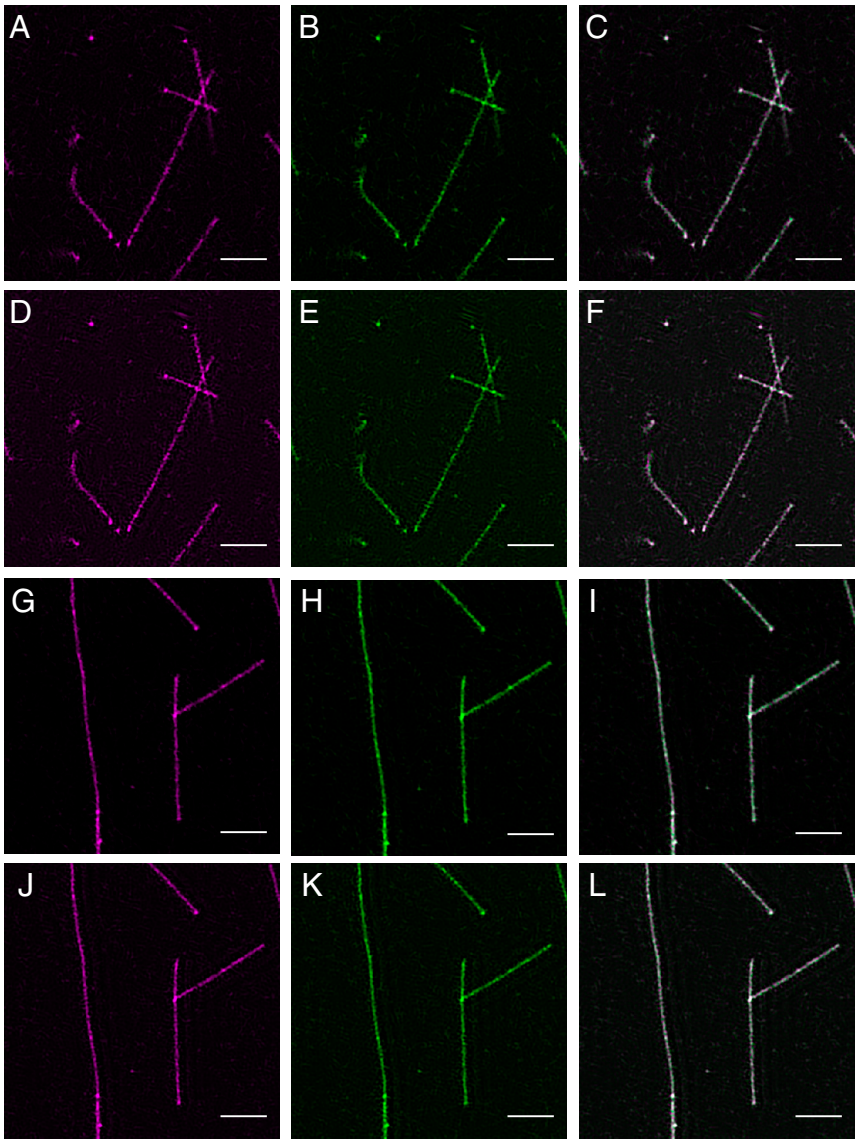

Fig. S6. Reproducibility of data. To understand how reproducible our data was, we repeated the NL-SIM imaging on a region of microtubules. Instead of taking the full datasets consecutively, we took an NL-SIM dataset in which we repeated the phase series for each pattern orientation. This was done to control for any photobleaching or drift-related effects. After imaging, we separated the interleaved datasets and processed each set individually. The first processed NL-SIM dataset (seven directions; five phases; $\eta = 5$) is shown in purple (*A*, *D*, *G*, and *J*), the second processed dataset is shown in green (*B*, *E*, *H*, and *K*), and merging the two appears white (*C*, *F*, *I*, and *L*). To simulate low labeling density, we used a streptavidin concentration of 0.2 mg/mL (*A*–*F*); to simulate dense labeling, we used 1 mg/mL streptavidin (*G*–*L*). Even though the overall shape of the microtubule is very reproducible in all images, the effect of the stochastic single molecules is more apparent at low streptavidin concentrations (*A*–*C*) as some of the fine structure along the microtubule appears only in one dataset. This is somewhat mitigated by using the image resulting from the off exposure as described in the *Materials and Methods* section of the main text (*D*–*F*). At high streptavidin concentrations, the effect of the single molecules is less apparent and the data highly reproducible (*G*–*I*). Combining the data from the off exposure has little effect (*J*–*L*). Scale bar, 1 μm.

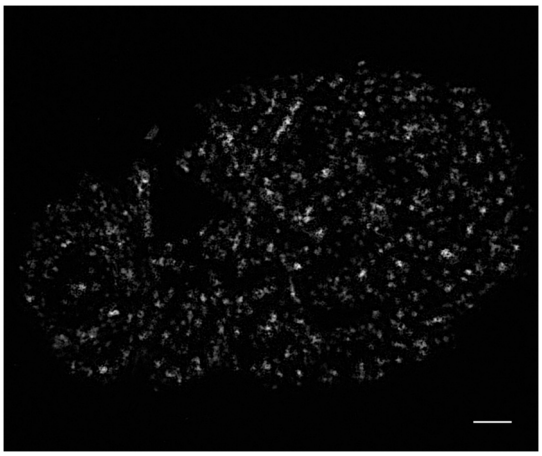

Fig. S7. POM121 in a second nucleus. We repeated the measurement in the main text on another nucleus and again saw a ring or pore-like structure in the POM121-Dronpa expressing cells. We included a subset of this data in Fig. 5. Scale bar, 1 μm.

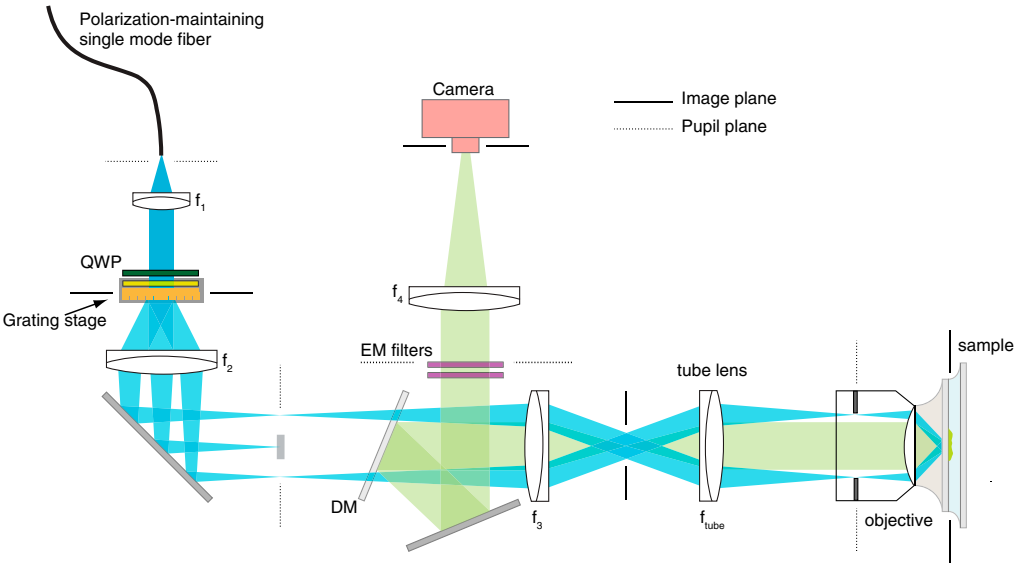

Fig. S8. Microscope setup. We designed a custom SIM-TIRF microscope. Light that was collimated from a single-mode polarization maintaining fiber ($N.A._{nominal} = 0.12$) was first passed through a quarter-wave plate (QWP) to produce circularly polarized light, and then through a custom phase grating with a period of 33.5 μm. The grating was mounted on a piezo-electric translational stage, which in turn was mounted on a rotational stage. This setup allowed the grating to be translated and rotated to produce all the necessary pattern phases and orientations. To maintain s-polarized light at all angle orientations, we mounted a wire polarizer that co-rotated with the grating. The central order from the diffraction grating was blocked at an intermediate pupil plane, and the +1 and −1 diffraction orders were refocused at the edges of the back focal plane of a 100× Zeiss 1.46 N.A. TIRF objective. The N.A. of the two side diffraction beams was designed to be 1.46, corresponding to a pattern period of 166 nm. The epifluorescence was collected, passed through a 1× Zeiss tube lens, and directed toward a camera using a custom multiband-pass dichroic mirror (DM) from Chroma. The dichroic mirror was designed to maintain the polarization state and minimize aberrations in the excitation light. Finally, the emission light was focused onto a 1,024 × 1,024 cooled CCD camera. (f_1: 50 mm; f_2: 150 mm; f_3: 150 mm; f_{tube}: $100 \times f_{obj}$; f_4: 400 mm; EM filters: Emission filters Semrock 525/40).

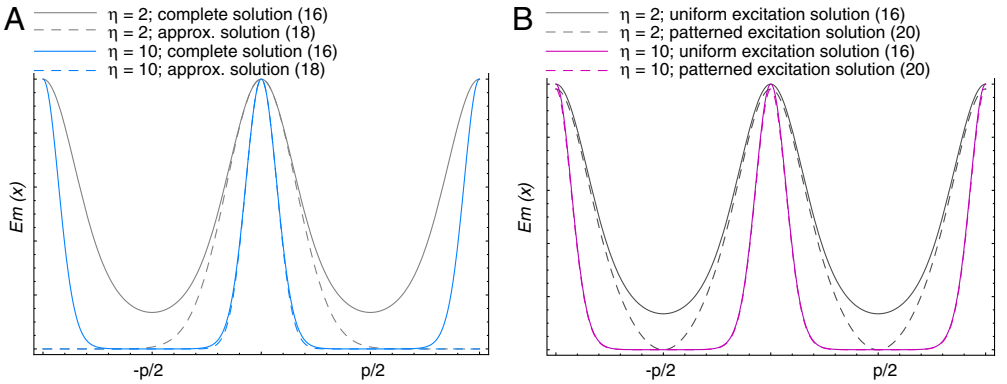

Fig. S9. Simulations. (*A*) The numerical approximation (dashed line) in Eq. **S18** agrees well with the complete solution in Eq. **S16** at moderate saturation (blue) but does not fully represent the solution at low saturation level (gray). (*B*) The effect of the patterned excitation (dashed) light can be seen at low saturation (gray) because the zero of the excitation light affects the nonzero trough of the patterned-on molecules (solid). At high saturation (pink), there is no effect of the patterned excitation light compared to uniform excitation.

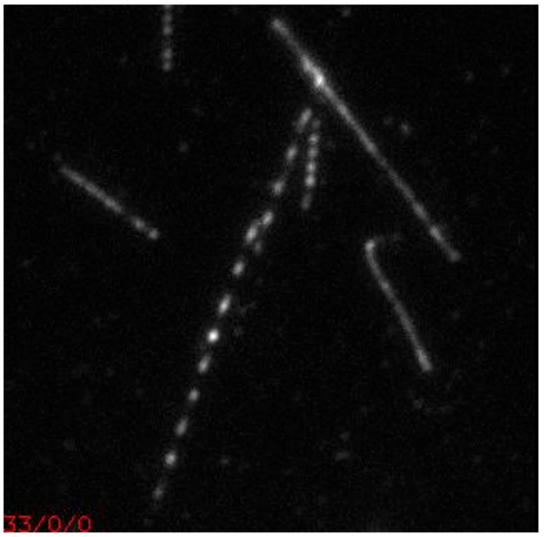

Movie S1. NL-SIM raw data. A subset of the raw data taken on Dronpa-coated microtubules is shown. The data consists of 63 images corresponding to seven phases and nine orientations of the illumination pattern. The moiré effect is easily visualized with the highly linear microtubules.
Movie S1 (MOV)